Waveguide-Integrated Compact Plasmonic Resonators for On-Chip Mid-Infrared Laser Spectroscopy

Journal:	*Nano Letters*
Manuscript ID	nl-2018-031563.R1
Manuscript Type:	Communication
Date Submitted by the Author:	n/a
Complete List of Authors:	Chen, Che; University of Minnesota Twin Cities, Electrical and Computer Eng. Mohr, Daniel; University of Minnesota, Electrical and Computer Engineering Choi, Han-Kyu; University of Minnesota College of Science and Engineering, Electrical and Computer Enginnering Yoo, Daehan; University of Minnesota, Electrical and Computer Engineering Li, Mo; University of Minnesota, Electrical and Computer Engineering Oh, Sang-Hyun; University of Minnesota, Electrical and Computer Engineering

Waveguide-Integrated Compact Plasmonic Resonators for On-Chip Mid-Infrared Laser Spectroscopy

Che Chen, Daniel A. Mohr, Han-Kyu Choi, Daehan Yoo, Mo Li*, Sang-Hyun Oh*

Department of Electrical and Computer Engineering, University of Minnesota, Minneapolis, Minnesota 55455, United States

*E-mail: moli@umn.edu and sang@umn.edu

Abstract

The integration of nanoplasmonic devices with a silicon photonic platform affords a new approach for efficient light delivery by combining the high field enhancement of plasmonics and the ultralow propagation loss of dielectric waveguides. Such a hybrid integration obviates the need for a bulky free-space optics setup and can lead to fully integrated, on-chip optical sensing systems. Here we demonstrate ultra-compact plasmonic resonators directly patterned atop a silicon waveguide for mid-infrared spectroscopic chemical sensing. The footprint of the plasmonic nanorod resonators is as small as 2 μm^2, yet they can couple with the mid-infrared waveguide mode efficiently. The plasmonic resonance is directly measured through the transmission spectrum of the waveguide, with a coupling efficiency greater than 70% and the field intensity enhancement factor of over 3600 relative to the evanescent waveguide field intensity. Using this hybrid device and a tunable mid-infrared laser source, surface-enhanced infrared absorption spectroscopy of both a thin PMMA film and an octadecanethiol monolayer are successfully demonstrated.

Keywords: Plasmonics, silicon photonics, waveguide, surface-enhanced infrared absorption (SEIRA), nanogap, optical parametric oscillator (OPO).

TOC Graphic

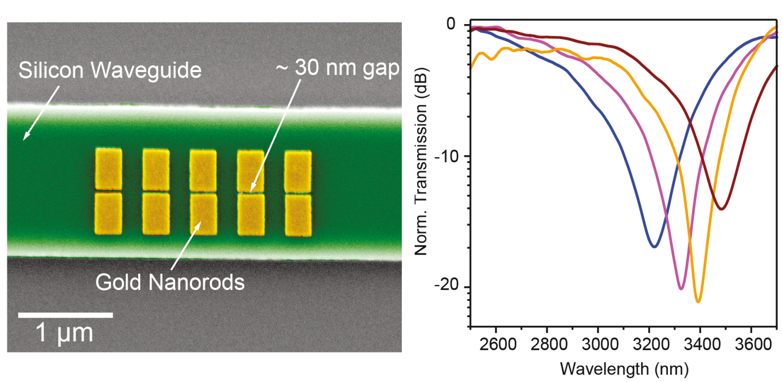

Metallic nanostructures can tightly confine electromagnetic waves below the diffraction limit and dramatically enhance light-matter interactions by harnessing surface plasmons. The sub-wavelength field localization and resonant field enhancement rendered by nanoplasmonic devices have significantly benefitted optical sensing technologies[1,2] such as surface-enhanced Raman scattering (SERS),[3–5] and surface-enhanced infrared absorption (SEIRA).[6–15] Among these methods, SEIRA directly measures absorption peaks related to molecular bonds in the infrared band and is capable of detecting and identifying a minute amount of analyte. For a wide range of applications from industrial chemical sensing to biomedical diagnosis, it is highly desirable to implement SEIRA as a portable, fully-integrated system in a miniaturized form-factor. Currently, however, SEIRA sensing is typically performed with a bulky table-top setup consisting of a Fourier Transform Infra-Red (FTIR) spectrometer coupled with a microscope. Such systems are not amenable to chip-scale miniaturization. Another limitation of performing SEIRA with a conventional FTIR system is its use of a low-brilliance thermal IR source (i.e. a Globar source), which also consumes high power. The inefficiency of the source requires a large number of plasmonic sensing elements (e.g. nanorods, bowtie antennas) and a long integration time to achieve sufficient signal-noise ratio, thus limiting both the chip size and the signal acquisition speed.

Unlike thermal IR sources, coherent IR sources such as quantum cascade lasers (QCL) and optical parametric oscillators (OPO) can generate output beams with much higher brilliance over a widely tunable spectral range.[16,17] Since chip-scale QCL,[18] OPO,[19] and mid-IR frequency combs[20] have become available in recent years, these coherent sources show great promise for SEIRA applications. Aside from the IR source, another technical challenge of SEIRA is the inefficiency of coupling the light from the source to nanoplasmonic resonators because of the mismatch between the diffraction-limited optical spot size and the deep-subwavelength plasmonic mode size in the nanostructures. For instance, most SEIRA measurement setups use a reflective (i.e. Schwarzschild) objective lens to focus IR light to a typical spot size of tens of micrometers,[17] which is much larger than the dimension of typical plasmonic sensors.

Fully integrated on-chip SEIRA systems can leverage the tremendous development of integrated photonics, which can be manufactured *en masse* in commercial foundries. Silicon waveguides can deliver light on-chip with very low propagation loss over a broad IR spectral range.[21–25] Placing photonic devices of different materials in the vicinity of a silicon waveguide enables efficient coupling with the evanescent field of the waveguide mode and thus heterogeneous integration to achieve new functionalities with impressive performances.[26–28] Hybridization of nanoplasmonics and silicon photonics has been conceived by many to combine plasmonics' strong field enhancement with silicon waveguide's optical mode confinement and low propagation loss. So far, there have been many successes in attempting such a hybrid approach in optical modulation,[29,30] photodetection,[31,32] mode conversion,[33,34] sensing,[35,36] and heat-assisted magnetic recording (HAMR).[37] In addition, the efficient coupling between plasmonic structures and silicon waveguides has been achieved for metallic nanotapers[38] and nanoparticle chains[39]. Specifically, for sensing applications, bowtie nanoantennas have been integrated on silicon nitride waveguides to realize on-chip SERS.[36] However, few hybrid waveguide-plasmonic devices have been demonstrated in the mid-IR range for SEIRA application, though a hybrid waveguide mode converter has been reported recently.[33]

In this letter, we experimentally demonstrate mid-IR SEIRA chemical sensing with an ultra-compact array of plasmonic nanorods directly integrated atop a silicon waveguide. Efficient coupling between the waveguide and an array of 5 pairs of nanorods with a footprint of only 2 μm^2 is achieved. This hybrid architecture offers two-stage enhancement of the optical field: the high-index silicon waveguide first confines mid-infrared light in a diffraction-limited guided optical mode, and subsequently the integrated plasmonic resonators couple the propagating mode to the gap plasmon modes tightly localized in the nanometer scale. The plasmonic resonators can boost the evanescent field amplitude of the waveguide mode by a factor of over 60. Using this plasmonics-waveguide hybrid device and a tunable mid-IR OPO source, we successfully detect multiple C-H bond absorption peaks for PMMA thin films and monolayer octadecanethiol (ODT).

Our measurement setup is illustrated in Figure 1a. A tunable OPO laser (M Squared, Firefly IR SW) covering the wavelength range from 2.5 to 3.7 μm is used as the coherent IR light source. The laser beam is first focused into a single-mode IR fiber (Thorlabs, ZrF_4 fiber patch cable, core diameter: 9 μm) with a reflective collimator, which can be omitted if the laser has fiber-coupled output. Next, the fiber output light is coupled into the input end of the waveguide with a butt-coupling configuration. Another multi-mode IR fiber (Thorlabs, InF_3 fiber patch cable, core diameter: 100 μm) collects light from the output end of the waveguide and transmits to a photodetector (see Figure S1 in the supplementary information for more details). The transmission spectrum of the waveguide is obtained by scanning the laser output wavelength while acquiring the output signal of the photodetector at the same time. A chopper (Stanford Research Systems, SR 540) and a lock-in amplifier (SR 830) are used to improve the signal-to-noise ratio.

The plasmonic-waveguide hybrid device is fabricated on a silicon-on-insulator (SOI) substrate with a 600 nm thick silicon device layer and a 3 μm thick buried oxide layer. The silicon rib waveguide is patterned with electron beam lithography (EBL) (Vistec EBPG 5000+) and etched with a reactive ion etching (RIE) process. The rib waveguide is 1600 nm in width (W), 400 nm in depth (D) and 200 nm in the thickness of the slab layer. The waveguide supports a fundamental TE mode in the measured wavelength range (Figure 1e) and is designed to reduce mode leakage into the SiO_2 layer underneath, which has non-negligible absorption in the mid-IR band. As shown in Figure 1a, the two ends of the waveguides are inversely tapered to a width of 120 nm to improve fiber-waveguide coupling efficiency and suppress Fabry–Pérot oscillation stemming from facet reflections. At the middle section and directly on the top of the waveguide (Figure 1a inset), five pairs of nanorods made of 3 nm Ti/35 nm Au with a narrow gap of ~30 nm are directly patterned with EBL, metal deposition, and lift-off processes. Precise alignment between the silicon waveguide and the nanorods is clearly shown in the SEM image of the device (Figure 1d).

Efficient optical coupling between the waveguide and the nanorod array can occur when the laser wavelength is tuned to the resonance of the nanorods, as our previous work showed.[40] As a result of the plasmonic enhancement, hotspots of the field are generated in the nanogaps as shown in Figures 1d and e. This resonant coupling results in strong dissipation of the guided mode due to metallic absorption and radiation from the nanorods and thus a suppressed transmission through the waveguide within the bandwidth of the resonance. When the wavelength is off-resonance, the propagating waveguide mode interacts with the nanorods weakly and only suffers from relatively weak broadband absorption and scattering. Because of the very small footprint of the nanorod array, the off-resonance loss is much smaller as compared to other devices with longer metallic structures.[33,39] Therefore, such an integrated configuration allows measuring the nanorods' resonance conveniently through the transmission spectrum of the waveguide, in much the same way as waveguide side-coupled dielectric resonators such as silicon micro-ring and photonic crystal cavities. Compared to dielectric resonators, metallic plasmonic resonators have a much smaller footprint and mode volume, but also low Q factors (typically <10 in the mid-IR). Both types of cavities/resonators have their advantages and shortcomings and should be evaluated depending on specific application requirements.

The nanorod array has multiple design parameters including length (*l*), period (*p*), width (*w*) and gap (*g*) as denoted in Figure 1f. These parameters collectively determine the resonant wavelength, the field enhancement factor, and the coupling strength with the silicon waveguide.[40,41] Specifically, since SEIRA signal increases with the square of the electric field amplitude, the most critical parameter among them is the nanogap width, which determines the field enhancement factor. Considering the fabrication precision and yield, we choose a gap size of 30 nm. To maximize the field enhancement factor, more advanced fabrication processes can be applied[15,42] to reduce the gap size to as small as 2-3 nm. The 3D finite-difference time-domain (FDTD) simulation in Figures 1d and e shows that, on resonance, the highest electric field intensity is in the nanogap between the center pair of nanorods, where the field amplitude enhancement factor is over 60 with respect to the evanescent field of the waveguide mode (1 nm above the waveguide top surface).

We design the resonance of the nanorod array to be within the spectral range of our laser source. Figure 2a shows the measured transmission spectra of the devices with changing nanorod length (*l*). To acquire the spectrum, the laser wavelength is scanned in steps of 10 nm. To acquire the measured spectra, we first measure the transmission spectrum of a waveguide without plasmonic elements as the baseline. Next, we measure the spectra of the integrated device with 5 pairs of nanorods on the same chip, which are then divided by the baseline from the first measurement. Finally, we normalize each spectrum to its maximal value for clear demonstration and comparison. A strong resonance peak can be observed in the spectrum. As the length of the nanorods increases and the period (*p*), width (*w*), and gap (*g*) remain fixed, it is observed that the resonance wavelength consistently red-shifts and the extinction ratio changes non-monotonically. When l = 420 nm, the extinction ratio reaches the highest value of over 20 dB. We note that the situation is quite different from that of a plasmonic perfect absorber[43,44] because in our devices reflection and scattering cannot be neglected. Our simulation in Figure S6(a) shows that when the resonance of the nanorod array is excited, of the total incident power in the waveguide, the nanorod arrays resonantly reflect 30% into the backward propagating waveguide mode, absorb 20 %, and scatter the rest downward into the oxide layer and upward into free-space. It is worth noting that, due to metallic damping, the wavelength at which the near-field intensity maximum is slightly red-shifted relative to the wavelength when far-field intensity is maximal[45,46]. Thus, the maximum electric field intensity (Figure 1f and g) indeed occurs at the wavelength near 3.5 µm, red-shifted from the wavelength position of maximum extinction near 3.3 µm as measured.

To fit the measured transmission spectra and understand the underlying mechanism of the change in extinction ratio, a theoretical model is derived. In devices with a long chain of metallic gold nanoparticles on top of a silicon waveguide, the chain is treated as a plasmonic waveguide to allow the use of coupled mode theory.[33,39,47] Our device, however, has a very short plasmonic device length and very high field enhancement, such that coupled mode theory is not appropriate. Instead, we treat our plasmonic array as a resonator[48,49] and use temporal coupled-mode theory to model the system.[50,51] With this approach, the transmission spectrum can be written as the following (the derivation can be found in supplementary information):

$$T = \frac{|s_{2-}|^2}{|s_{1+}|^2} = |t_0|^2 + \frac{-\frac{2\beta}{\tau_{te}}(w-w_0) + \left(\frac{1}{\tau_{te}}\right)^2 + \frac{2\alpha}{\tau\tau_{te}}}{(w-w_0)^2 + \left(\frac{1}{\tau}\right)^2} \quad (1)$$

Here s_{2-} and s_{1+} represent the outgoing amplitude from the output waveguide and incoming amplitude from the input waveguide, respectively. ω_0 is the resonance frequency of the resonator, $1/\tau_{te}$ represents the resonator's total external coupling rate to the waveguide mode, and $1/\tau$ is the total loss of the resonator and corresponds to the linewidth of the resonance. In addition, we introduce a complex, frequency-independent off-resonance transmission coefficient $t_0=\alpha+j\beta$ to account for the broadband damping (α) and the phase shift (β) caused by non-resonant interaction with the nanorods. We can extract the parameters: ω_0, τ_{te}, τ, α, β by fitting the measured transmission curves in Figure 2a. The extracted values of $1/\tau$ and $1/\tau_{te}$ are plotted in Figure 2b with respect to different nanorod lengths. According to our detailed analysis (in supplementary information), when the ratio $\eta=\tau_{te}/\tau$ equals $-\alpha/(\alpha^2+\beta^2)$, the transmission spectrum has its minimal value and thus the highest extinction ratio. Specifically, when l=420 nm, the ratio η is closest to this critical value, thus the measured spectrum shows the highest extinction ratio (figure 2a). Because of the complex t_0, the resonance is slightly distorted from an ideal Lorentz resonance lineshape.[52] The very high extinction ratio of greater than 20 dB achieved when l = 420 nm indicates that, other than a non-resonance loss of $1-|t_0|^2$, more than 99% of the power in the waveguide mode is coupled to the resonance mode of the nanorods. Our measurement results, as well as the simulation results in Figure 2c, show that the non-resonance loss $1-|t_0|^2$ is typically 30% so that an on-resonance, waveguide-plasmonic coupling efficiency of 70% is achieved in our device.

To demonstrate on-chip SEIRA sensing using our waveguide-integrated hybrid device, poly(methyl methacrylate) (PMMA) was used as a model analyte because it is a widely used electron beam resist, which can be patterned with nanometer accuracy, and has a thoroughly characterized absorption spectrum in the infrared. We first performed simulations to examine the feasibility. In the simulation, the PMMA was included as a 200-nm thick layer conformally covering only the nanorods (3 μm ×1.6 μm in the area) and its complex refractive index was used. The result in Figure 2c apparently shows multiple absorption peaks due to PMMA in this band. As a comparison, for a waveguide covered with the same area of PMMA, but without the nanorods, its transmission spectrum shows no discernable spectroscopic features from PMMA absorption. These results verify that a bare waveguide does not provide enough field enhancement to sense a small amount of analyte localized on it, while waveguide-integrated plasmonic resonators can detect them via SEIRA.

In our experiments, the PMMA was patterned on the nanorods as illustrated in Figure 3a and shown in the optical microscope image in Figure 3b. First, the entire chip was spin-coated with PMMA (4% in chlorobenzene solvent) and then baked on a hotplate at 120 ºC for 16 min, with the precaution to prevent heat-induced deformation of the gold nanorods. We then used EBL to pattern the PMMA layer into a patch only covering the nanorods. However, this process usually left a very thin layer of organic residue on the surface of the entire chip. Thus, an additional O_2 plasma cleaning process was necessary to remove the residue. The O_2 cleaning step also thins down the PMMA on the nanorods, so it can be used to control the PMMA thickness. The thickness of PMMA was determined with atomic force microscopy (AFM) as in Figure 3c. The initial PMMA film thickness is 230 nm. The optical micrograph in Figure 3b shows that only the nanorod array area is covered with a PMMA layer.

SEIRA measurement results are presented in Figure 3d. The top and middle panels show the transmission spectra of the device with PMMA film thickness of 230 nm and 160 nm, respectively. The asymmetric least square smoothing (AsLSS) method[53] is used to create the baselines for the measured curves. Compared to the transmission spectrum of the same device with no PMMA analyte (in the bottom panel), three spectroscopic changes can be observed due to PMMA: the redshift of the resonance peak, the reduction of the extinction ratio, and the appearance of multiple absorption peaks within the plasmonic resonance. The former two changes are simply due to the refractive index of PMMA, which results in shifting the resonance to longer wavelengths and modifying the waveguide-nanorod array coupling strength. The third change is the hallmark of SEIRA sensing. The infrared absorption peaks are from the vibrational modes of the C-H bonds in PMMA molecules and they interfere with the broader plasmonic resonance of the nanorods to form the multiple resonance peaks in the transmission spectra.

To verify that the absorption peaks are indeed from the PMMA film, we used FTIR to measure the absorption spectrum of a 400 nm PMMA film coated on a silicon wafer. The FTIR transmission spectrum can be precisely fitted with four individual Lorentz peaks, which are known to be induced by different vibrational modes of the chemical bonds in the PMMA molecules.[54] The detailed assignments of the absorption peaks are listed in Table 1. In Figure 3e, we compare the FTIR results with the SEIRA results, which is normalized by the AsLSS fitted baseline. The SEIRA absorption spectrum (middle panel, Figure 3e) clearly shows three peaks, corresponding to peak 1), 3) and 4) in the FIIR spectrum. Their wavelength positions agree reasonably well with the FTIR spectrum despite small deviations likely due to the inaccuracy of the OPO laser output wavelength. The relative strengths between the peaks also agree with the FTIR result. The shoulder peak (peak 2), however, is hardly resolvable because of its close proximity to the nearby strong absorption peak (peak 3). The observation of the three distinct peaks in our SEIRA measurement is made possible by the resonant field enhancement afforded by the gold nanorod array. It is clear that thicker PMMA layer (230 nm) induces a larger red-shift of the plasmonic resonance and generate stronger SEIRA absorption peaks than the thinner PMMA layer (160 nm). It indicates that the probing range is more than 160 nm from the nanorods' surface with the evanescent field of the surface plasmon.[55,56] In a control experiment to verify the necessity of field enhancement by the nanorods, we patterned the same area of 200 nm thick PMMA on a bare silicon waveguide and performed the same measurement. The measured spectrum, shown in the bottom panel of Figure 3e, presents no discernable absorption peaks, in agreement with the simulation result in Figure 2c. Apparently, the direct interaction between the evanescent field of the waveguide mode and such a thin PMMA film is insufficient to generate absorption peaks above the noise background. It is thus confirmed that the observed absorption peaks are enabled by the surface enhancement of the plasmonic resonators.

Next, we demonstrate SEIRA measurement of a self-assembled monolayer of ODT molecules on the surface of the gold nanorods. To do so, the device was incubated in ODT solution (1 μM in ethanol solution) overnight before performing SEIRA measurement. Comparing the transmission spectra measured before and after ODT coating in Figure 4a, a small redshift of the resonance peak is observed. After normalization to the fitted baseline of the plasmonic resonance, two absorption peaks become clearly visible in Figure 4b and c. Compared with the reported ODT absorption spectrum, the stronger peak at 3508 nm can be attributed to the symmetric stretching mode of the CH_2 bond (2850 cm^{-1}) and the weaker peak near 3460 nm to the Fermi-resonant symmetric stretching mode (2878 cm^{-1}) of the CH_3 bond.[10] The thickness (2.4 nm) of the ODT monolayer is ~1400 times smaller than the free-space wavelength and the number of ODT molecules in the gap region (hotspot) is 2.4×10^5. Nevertheless, our device still generates absorption peaks with a signal-to-noise ratio better than 3. The intrinsically weak absorption of the C-H bond in the measured short-wavelength mid-IR band (2.5-3.7 μm), limited by the range of our OPO laser, is in part responsible for the weakness of the acquired signal. Therefore, our results demonstrate the potential of on-chip SEIRA sensing with a waveguide-integrated architecture.

To further improve the sensitivity of SEIRA sensing, two possible approaches can be taken. First, the field enhancement factor of the plasmonic resonator can be further improved by reducing the center gap width to only a few nm with more advanced fabrication methods[13,42,57] or using a coaxial aperture structure with higher field confinement.[12,40] Second, SEIRA sensing can be performed in the long-wavelength mid-IR band around 5 μm range, which is the "fingerprint" range of organic molecules. In this spectral range, the C=O bond has ~ 5 times stronger absorption than that of the C-H bond in 3.5 μm band. However, to operate in the long-wavelength mid-IR range, the current silicon waveguide on an SOI substrate will suffer a high propagation loss due to the stronger absorption of the SiO_2 cladding layer. Low-loss waveguides can be fabricated with different material platforms, such as chalcogenide glasses or silicon on calcium fluoride substrate.[58,59]

In conclusion, we have achieved highly efficient coupling to plasmonic resonators by directly integrating them on top of a mid-IR silicon waveguide. In our hybrid approach, the plasmonic resonance can be conveniently measured through the waveguide transmission and exhibit an extinction ratio of more than 20 dB. With this waveguide-plasmonic hybrid device, we demonstrate SEIRA sensing of both PMMA material and an ODT monolayer by measuring their C-H bond absorption peaks in the mid-IR band. This prototype waveguide-integrated SEIRA platform is an important step forward towards building a fully integrated and miniaturized SEIRA system. With the advancement of on-chip QCL and photodetectors for light generation and detection, along with microfluidic packaging for site-specific analyte delivery, it will be possible to achieve an integrated and multiplexed sensing system in a single package that is greatly smaller than conventional FTIR/microscope systems. Benefiting from the efficient coupling with the waveguide mode, this compact plasmonic device can also be used as an optical resonator as an alternative to dielectric cavities for on-chip nonlinear optics[60] and optical communications.[29] The strong interaction between a plasmonic resonator and a waveguide in the mid-IR range could potentially reveal fundamental physics including plasmon hybridization,[61] strong coupling of plasmon-phonon,[62]and waveguide integrated parity-time metamaterial.[63] Moreover, in addition to simple plasmonic resonators, more complicated and versatile metasurfaces[64,65] may enable novel functionalities (e.g. multi-resonant and low-loss sensors) on such a hybrid platform.

ASSOCIATED CONTENT

Supporting Information

The Supporting Information is available free of charge on the ACS Publications website at DOI: xxxxxxxx

Corresponding Authors

E-mail: moli@umn.edu, sang@umn.edu

Notes: The authors declare no competing financial interest.

ACKNOWLEDGMENTS

We thank Dr. Huan Li for the helpful discussion on the coupled mode theory. This work was supported by the National Science Foundation (NSF Award No. ECCS 1809240 to M.L. and S.-H.O.; ECCS-1708768 for C.C., M.L.; ECCS-1610333 for D.A.M., H.-K.C., S.-H.O.). D.A.M. and S.-H.O. also acknowledge support from Seagate through the MINT consortium. Device fabrication was carried out at the Minnesota Nanofabrication Center, which receives partial support from the NSF through the National Nanotechnology Coordinated Infrastructure (NNCI) program. The authors also used resources at the Characterization Facility, which is a member of the NSF-funded Materials Research Facilities Network via the NSF MRSEC program.

References

(1) Lal, S.; Link, S.; Halas, N. J. *Nat. Photonics* **2007**, *1*, 641–648.

(2) Brolo, A. *Nat. Photonics* **2012**, *6*, 709–713.

(3) Haynes, C. L.; McFarland, A. D.; Duyne, R. P. Van. *Anal. Chem.* **2005**, *77*, 338 A-346 A.

(4) Talley, C. E.; Jackson, J. B.; Oubre, C.; Grady, N. K.; Hollars, C. W.; Lane, S. M.; Huser, T. R.; Nordlander, P.; Halas, N. J. *Nano Lett.* **2005**, *5*, 1569–1574.

(5) Halas, N. J. *Nano Lett.* **2010**, *10*, 3816–3822.

(6) Neubrech, F.; Pucci, A.; Cornelius, T. W.; Karim, S.; García-Etxarri, A.; Aizpurua, J. *Phys. Rev. Lett.* **2008**, *101*, 157403.

(7) Lal, S.; Grady, N. K.; Kundu, J.; Levin, C. S.; Lassiter, J. B.; Halas, N. J. *Chem. Soc. Rev.* **2008**, *37*, 898.

(8) Cubukcu, E.; Zhang, S.; Park, Y.-S.; Bartal, G.; Zhang, X. *Appl. Phys. Lett.* **2009**, *95*, 043113.

(9) Adato, R.; Yanik, A. A.; Amsden, J. J.; Kaplan, D. L.; Omenetto, F. G.; Hong, M. K.; Erramilli, S.; Altug, H. *Proc. Natl. Acad. Sci.* **2009**, *106*, 19227–19232.

(10) Brown, L. V; Yang, X.; Zhao, K.; Zheng, B. Y.; Nordlander, P.; Halas, N. J. *Nano Lett.* **2015**, *15*, 1272–1280.

(11) Braun, A.; Maier, S. A. *ACS Sensors* **2016**, *1*, 1155–1162.

(12) Yoo, D.; Nguyen, N.-C.; Martin-Moreno, L.; Mohr, D. A.; Carretero-Palacios, S.; Shaver, J.; Peraire, J.; Ebbesen, T. W.; Oh, S.-H. *Nano Lett.* **2016**, *16*, 2040–2046.

(13) Ji, D.; Cheney, A.; Zhang, N.; Song, H.; Gao, J.; Zeng, X.; Hu, H.; Jiang, S.; Yu, Z.; Gan, Q. *Adv. Opt. Mater.* **2017**, *5*, 1700223.

(14) Neubrech, F.; Huck, C.; Weber, K.; Pucci, A.; Giessen, H. *Chem. Rev*. **2017**, *117*, 5110–5145.

(15) Yoo, D.; Mohr, D. A.; Vidal-Codina, F.; John-Herpin, A.; Jo, M.; Kim, S.; Matson, J.;

Caldwell, J. D.; Jeon, H.; Nguyen, N. C.; Martin-Moreno, L.; Peraire, J.; Altug, H.; Oh, S. H. *Nano Lett.* **2018**, *18*, 1930–1936.

(16) Heydari, D.; Bai, Y.; Bandyopadhyay, N.; Slivken, S.; Razeghi, M. *Appl. Phys. Lett.* **2015**, *106*, 091105.

(17) Steinle, T.; Neubrech, F.; Steinmann, A.; Yin, X.; Giessen, H. *Opt. Express* **2015**, *23*, 11105.

(18) Spott, A.; Peters, J.; Davenport, M. L.; Stanton, E. J.; Merritt, C. D.; Bewley, W. W.; Vurgaftman, I.; Kim, C. S.; Meyer, J. R.; Kirch, J.; Mawst, L. J.; Botez, D.; Bowers, J. E. *Optica* **2016**, *3*, 545.

(19) Levy, J. S.; Gondarenko, A.; Foster, M. A.; Turner-Foster, A. C.; Gaeta, A. L.; Lipson, M. *Nat. Photonics* **2010**, *4*, 37–40.

(20) Griffith, A. G.; Lau, R. K. W.; Cardenas, J.; Okawachi, Y.; Mohanty, A.; Fain, R.; Lee, Y. H. D.; Yu, M.; Phare, C. T.; Poitras, C. B.; Gaeta, A. L.; Lipson, M. *Nat. Commun.* **2015**, *6*, 6299.

(21) Reimer, C.; Nedeljkovic, M.; Stothard, D. J. M.; Esnault, M. O. S.; Reardon, C.; O'Faolain, L.; Dunn, M.; Mashanovich, G. Z.; Krauss, T. F. *Opt. Express* **2012**, *20*, 29361.

(22) Mashanovich, G. Z.; Milošević, M. M.; Nedeljkovic, M.; Owens, N.; Xiong, B.; Teo, E. J.; Hu, Y. *Opt. Express* **2011**, *19*, 7112–7119.

(23) Zou, Y.; Chakravarty, S.; Chen, R. T. *Appl. Phys. Lett.* **2015**, *107*, 081109.

(24) Dong, B.; Guo, X.; Ho, C. P.; Li, B.; Wang, H.; Lee, C.; Luo, X.; Lo, G.-Q. *IEEE Photonics J.* **2017**, *9*, 4501410.

(25) Miller, S. A.; Yu, M.; Ji, X.; Griffith, A. G.; Cardenas, J.; Gaeta, A. L.; Lipson, M. *Optica* **2017**, *4*, 707.

(26) Youngblood, N.; Chen, C.; Koester, S. J.; Li, M. *Nat. Photonics* **2015**, *9*, 249–252.

(27) Liu, M.; Yin, X.; Ulin-Avila, E.; Geng, B.; Zentgraf, T.; Ju, L.; Wang, F.; Zhang, X. *Nature* **2011**, *474*, 64–67.

(28) Bie, Y.-Q.; Grosso, G.; Heuck, M.; Furchi, M. M.; Cao, Y.; Zheng, J.; Bunandar, D.; Navarro-Moratalla, E.; Zhou, L.; Efetov, D. K.; Taniguchi, T.; Watanabe, K.; Kong, J.; Englund, D.; Jarillo-Herrero, P. *Nat. Nanotechnol.* **2017**, *12*, 1124–1129.

(29) Haffner, C.; Chelladurai, D.; Fedoryshyn, Y.; Josten, A.; Baeuerle, B.; Heni, W.; Watanabe, T.; Cui, T.; Cheng, B.; Saha, S.; Elder, D. L.; Dalton, L. R.; Boltasseva, A.; Shalaev, V. M.; Kinsey, N.; Leuthold, J. *Nature* **2018**, *556*, 483–486.

(30) Haffner, C.; Heni, W.; Fedoryshyn, Y.; Niegemann, J.; Melikyan, A.; Elder, D. L.; Baeuerle, B.; Salamin, Y.; Josten, A.; Koch, U.; Hoessbacher, C.; Ducry, F.; Juchli, L.; Emboras, A.; Hillerkuss, D.; Kohl, M.; Dalton, L. R.; Hafner, C.; Leuthold, J. *Nat. Photonics* **2015**, *9*, 525–528.

(31) Goykhman, I.; Sassi, U.; Desiatov, B.; Mazurski, N.; Milana, S.; De Fazio, D.; Eiden, A.; Khurgin, J.; Shappir, J.; Levy, U.; Ferrari, A. C. *Nano Lett.* **2016**, *16*, 3005–3013.

(32) Chen, C.; Youngblood, N.; Peng, R.; Yoo, D.; Mohr, D. A.; Johnson, T. W.; Oh, S. H.; Li, M. *Nano Lett.* **2017**, *17*, 985–991.

(33) Li, Z.; Kim, M. H.; Wang, C.; Han, Z.; Shrestha, S.; Overvig, A. C.; Lu, M.; Stein, A.; Agarwal, A. M.; Lončar, M.; Yu, N. *Nat. Nanotechnol.* **2017**, *12*, 675–683.

(34) Ono, M.; Taniyama, H.; Xu, H.; Tsunekawa, M.; Kuramochi, E.; Nozaki, K.; Notomi, M. *Optica* **2016**, *3*, 999.

(35) Chamanzar, M.; Xia, Z.; Yegnanarayanan, S.; Adibi, A. *Opt. Express* **2013**, *21*, 32086.

(36) Peyskens, F.; Dhakal, A.; Van Dorpe, P.; Le Thomas, N.; Baets, R. *ACS Photonics* **2016**, *3*, 102–108.

(37) Challener, W. A.; Peng, C.; Itagi, A. V.; Karns, D.; Peng, W.; Peng, Y.; Yang, X.; Zhu, X.; Gokemeijer, N. J.; Hsia, Y.-T.; Ju, G.; Rottmayer, R. E.; Seigler, M. A.; Gage, E. C. *Nat. Photonics* **2009**, *3*, 220–224.

(38) Luo, Y.; Chamanzar, M.; Apuzzo, A.; Salas-Montiel, R.; Nguyen, K. N.; Blaize, S.; Adibi, A. *Nano Lett.* **2015**, *15*, 849–856.

(39) Gogol, P.; Aassime, A.; Chelnokov, A.; Apuzzo, A.; Blaize, S.; Lourtioz, J.-M. *Nano Lett.*

2012, *12*, 1032–1037.

(40) Mohr, D. A.; Yoo, D.; Chen, C.; Li, M.; Oh, S.-H. *Opt. Express* **2018**, *26*, 23540.

(41) Weber, D.; Albella, P.; Alonso-González, P.; Neubrech, F.; Gui, H.; Nagao, T.; Hillenbrand, R.; Aizpurua, J.; Pucci, A. *Opt. Express* **2011**, *19*, 15047.

(42) Dong, L.; Yang, X.; Zhang, C.; Cerjan, B.; Zhou, L.; Tseng, M. L.; Zhang, Y.; Alabastri, A.; Nordlander, P.; Halas, N. J. *Nano Lett.* **2017**, *17*, 5768–5774.

(43) Chen, B.; Bruck, R.; Traviss, D.; Khokhar, A. Z.; Reynolds, S.; Thomson, D. J.; Mashanovich, G. Z.; Reed, G. T.; Muskens, O. L. *Nano Lett.* **2018**, *18*, 610–617.

(44) Tittl, A.; Mai, P.; Taubert, R.; Dregely, D.; Liu, N.; Giessen, H. *Nano Lett.* **2011**, *11*, 4366–4369.

(45) Alonso-González, P.; Albella, P.; Neubrech, F.; Huck, C.; Chen, J.; Golmar, F.; Casanova, F.; Hueso, L. E.; Pucci, A.; Aizpurua, J.; Hillenbrand, R. *Phys. Rev. Lett.* **2013**, *110*, 203902.

(46) Zuloaga, J.; Nordlander, P. *Nano Lett.* **2011**, *11*, 1280–1283.

(47) Apuzzo, A.; Février, M.; Salas-Montiel, R.; Bruyant, A.; Chelnokov, A.; Lérondel, G.; Dagens, B.; Blaize, S. *Nano Lett.* **2013**, *13*, 1000–1006.

(48) Giannini, V.; Francescato, Y.; Amrania, H.; Phillips, C. C.; Maier, S. A. *Nano Lett.* **2011**, *11*, 2835–2840.

(49) Cubukcu, E.; Capasso, F. *Appl. Phys. Lett.* **2009**, *95*, 201101.

(50) Fan, S.; Suh, W.; Joannopoulos, J. D. *J. Opt. Soc. Am. A* **2003**, *20*, 569.

(51) Joannopoulos, J. D.; Johnson, S. G.; Winn, J. N.; Meade, R. D. *Photonic Crystals: Molding the Flow of Light*, 2 edition.; Princeton University Press: Princeton, **2008**.

(52) Suh, W.; Wang, Z.; Fan, S. *IEEE J. Quantum Electron.* **2004**, *40*, 1511–1518.

(53) Eilers, P. H. C. *Anal. Chem.* **2003**, *75*, 3631–3636.

(54) Willis, H. A.; Zichy, V. J. I.; Hendra, P. J. *Polymer (Guildf).* **1969**, *10*, 737–746.

(55) Limaj, O.; Etezadi, D.; Wittenberg, N. J.; Rodrigo, D.; Yoo, D.; Oh, S.-H.; Altug, H. *Nano Lett.* **2016**, *16*, 1502–1508.

(56) Bochterle, J.; Neubrech, F.; Nagao, T.; Pucci, A. *ACS Nano* **2012**, *6*, 10917–10923.

(57) Chen, X.; Ciracì, C.; Smith, D. R.; Oh, S. H. *Nano Lett.* **2015**, *15*, 107–113.

(58) Chen, Y.; Lin, H.; Hu, J.; Li, M. *ACS Nano* **2014**, *8*, 6955–6961.

(59) Yu, Y.; Gai, X.; Ma, P.; Vu, K.; Yang, Z.; Wang, R.; Choi, D.-Y.; Madden, S.; Luther-Davies, B. *Opt. Lett.* **2016**, *41*, 958.

(60) Nielsen, M. P.; Shi, X.; Dichtl, P.; Maier, S. A.; Oulton, R. F. *Science.* **2017**, *358*, 1179–1181.

(61) Prodan, E.; Radloff, C.; Halas, N. J.; Nordlander, P. *Science.* **2003**, *302*, 419–422.

(62) Caldwell, J. D.; Lindsay, L.; Giannini, V.; Vurgaftman, I.; Reinecke, T. L.; Maier, S. A.; Glembocki, O. J. *Nanophotonics* **2015**, *4*, 44–68.

(63) Feng, L.; Xu, Y. L.; Fegadolli, W. S.; Lu, M. H.; Oliveira, J. E. B.; Almeida, V. R.; Chen, Y. F.; Scherer, A. *Nat. Mater.* **2013**, *12*, 108–113.

(64) Rodrigo, D.; Tittl, A.; Ait-Bouziad, N.; John-Herpin, A.; Limaj, O.; Kelly, C.; Yoo, D.; Wittenberg, N. J.; Oh, S.-H.; Lashuel, H. A.; Altug, H. *Nat. Commun.* **2018**, *9*, 2160.

(65) Tittl, A.; Leitis, A.; Liu, M.; Yesilkoy, F.; Choi, D.-Y.; Neshev, D. N.; Kivshar, Y. S.; Altug, H. *Science.* **2018**, *360*, 1105–1109.

Table 1. Absorption peak positions, strengths and assignments of PMMA in the infrared range (~ 3.5 μm). v_s and v_a represent symmetric and antisymmetric stretching vibration, respectively.

Peak position	**Stength**	**Assignment**
2850 cm^{-1} (3508 nm)	very weak	combined band involving the $O-CH_3$
2915 cm^{-1} (3430 nm)	weak shoulder	combined band involving the $O-CH_3$ and $v_s(CH_2)$
2948 cm^{-1} (3392 nm)	strong	v_s(C-H) of $O-CH_3$ with v_s(C-H) of $\alpha-CH_3$ and $v_a(CH_2)$
2995 cm^{-1} (3339 nm)	medium	v_a(C-H) of $O-CH_3$ and v_a(C-H) of $\alpha-CH_3$

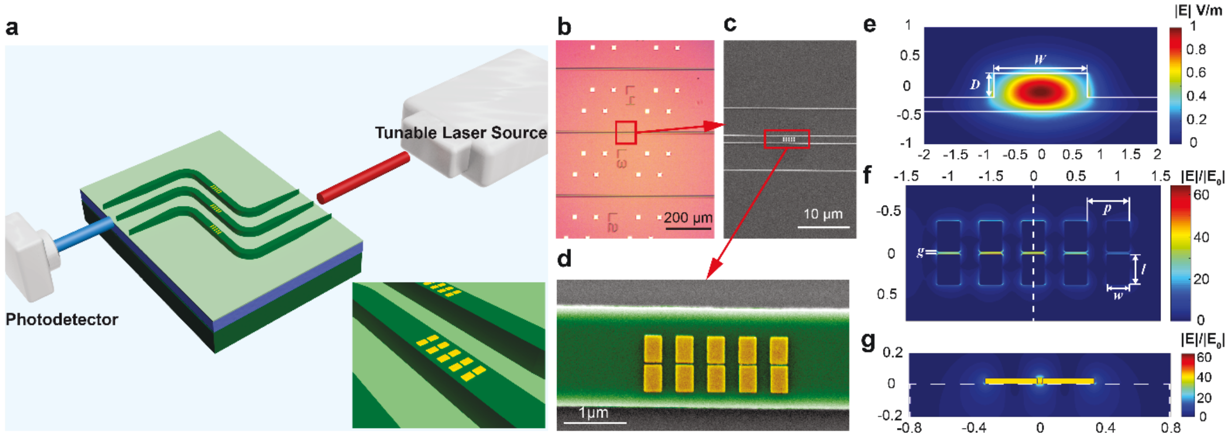

Figure 1. (a) 3D artistic illustration of the chip and the simplified measurement setup. Chopper and lock-in amplifier used in the experiment are not shown. Inset: zoom-in view of the nanorod array integrated on the waveguide. (b) Optical microscope image of the chip including multiple waveguides. (c) (d) Scanning electron microscope (SEM) image of the fabricated device. (e) Cross-sectional view of the simulated electric field distribution of the waveguide fundamental TE mode at 3.5 μm wavelength. *D* and *W* are the rib waveguide depth and width, respectively. (f) Top-view of the normalized electric field distribution (of the plane 1 nm above waveguide top surface) at the plasmonic resonant wavelength. The parameters of the nanorods are labeled as *p*, *l*, *w* and *g*, representing the nanorods' period, length, width and gap, respectively. (g) Cross-sectional view of the device sliced at the dashed line in (f) with the normalized electric field distribution at the resonance wavelength. The silicon waveguide is outlined with dashed line box. Note: the unit of coordinates in (e) (f) (g) is micrometer.

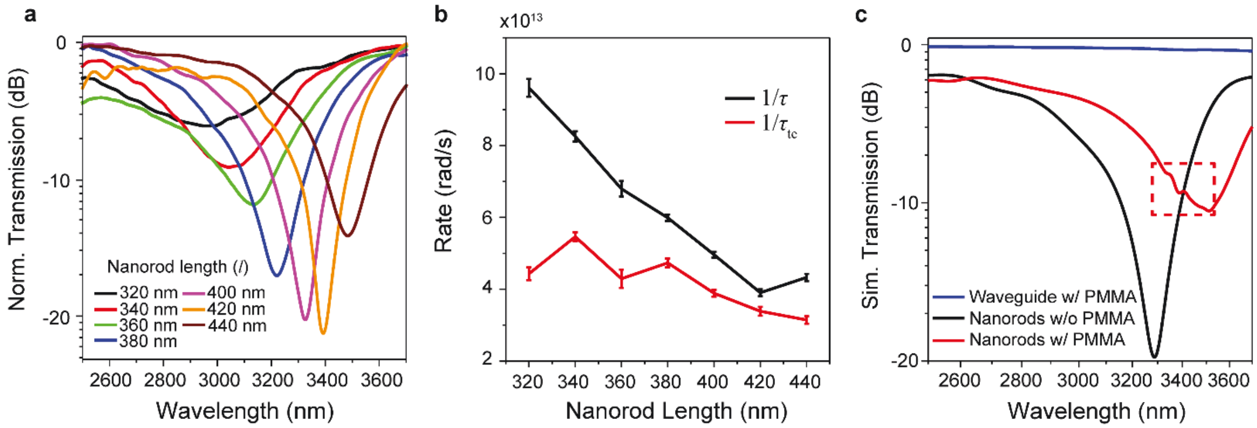

Figure 2. (a) Waveguide transmission spectra of devices with a fixed gap width of ~30 nm and varying nanorod lengths. The wavelength is scanned in steps of 10 nm. (b) Coupling parameters extracted by fitting the transmission spectrum of each nanorod length. $1/\tau$ and $1/\tau_{\mathrm{te}}$ represent total loss and total external loss of the waveguide-resonator coupled system, respectively. (c) FDTD-simulated transmission spectra of a reference waveguide-nanorod array device, the same device covered with 200 nm PMMA, and a bare waveguide (no nanorods) with a rectangular PMMA patch. The absorption peaks of PMMA are clearly visible (in the dashed line box) in the hybrid waveguide-resonator device.

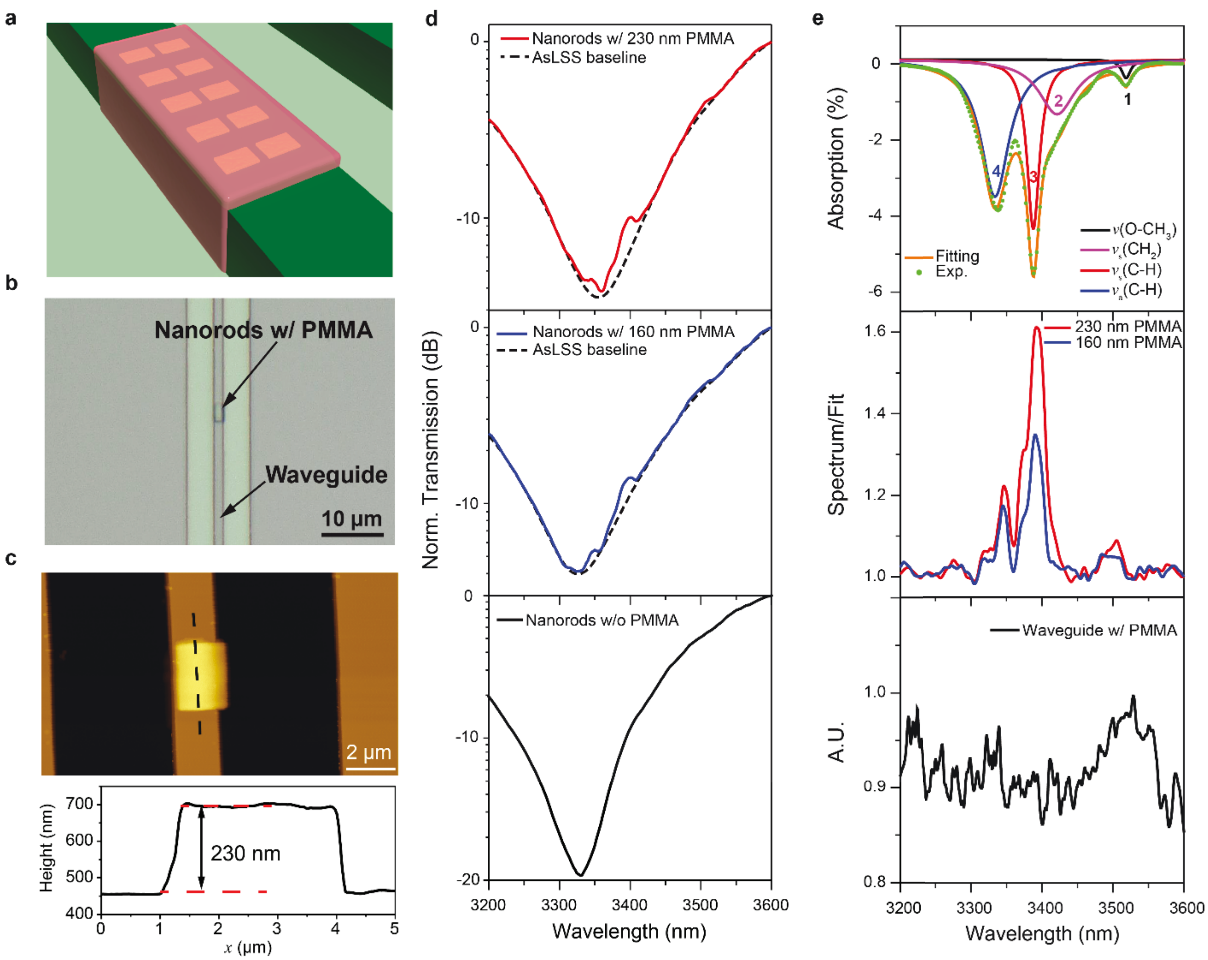

Figure 3. (a) The 3D illustration of PMMA analyte on top of metallic nanorods. (b) Optical microscope image of the waveguide-nanorod array device after PMMA patterning. (c) AFM image of the PMMA film on metallic nanorods. Lower panel: crosscut of the height profile of the film (~230 nm thickness). (d) Top and middle panel: transmission spectrum of nanorods covered with PMMA of ~230/160 nm thicknesses and the baselines extracted with the AsLSS method. Bottom panel: the spectrum of the same device without PMMA. The wavelength scan step is 2 nm. (e) Top panel: the FTIR absorption spectrum of 400 nm thick PMMA film on a double-polished silicon wafer. Middle panel: absorption spectra for different thicknesses of PMMA in (d) after normalization to the baselines. Bottom panel: transmission spectrum of a bare waveguide without nanorods and after adding a rectangular patch of 200 nm-thick PMMA.

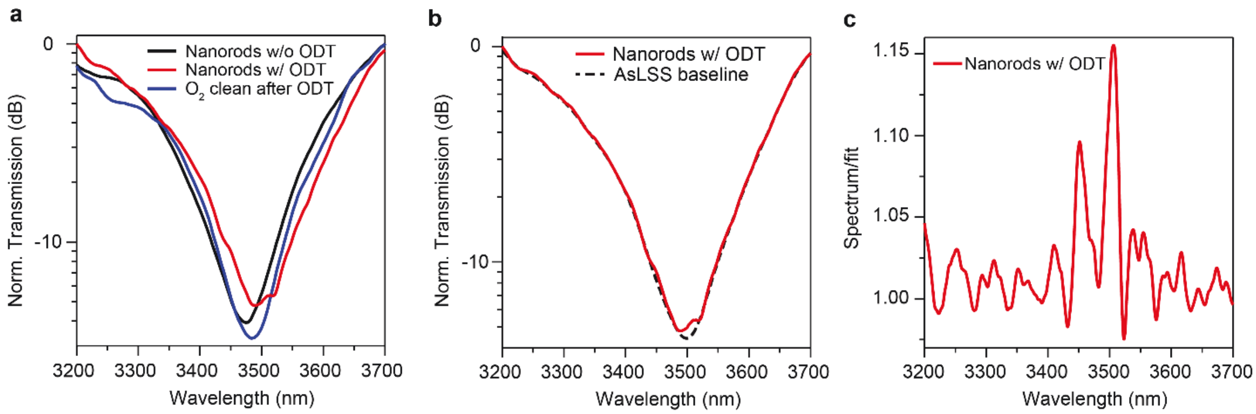

Figure 4. (a) The transmission spectra of the device at three different stages of the ODT sensing experiment: clean device before ODT coating, device with an ODT monolayer, and device cleaned by O_2 plasma after ODT coating and measurement. (b) The transmission spectrum of the same device after coating with an ODT monolayer. (c) The SEIRA spectrum of the ODT monolayer in (b), after normalization by the baseline, shows two prominent absorption peaks.